32ND INTERNATIONAL COSMIC RAY CONFERENCE, BEIJING 2011

Highlights from the ARGO-YBJ experiment

BENEDETTO D'ETTORRE PIAZZOLI[1] FOR THE ARGO-YBJ COLLABORATION
[1]*Dipartimento di Fisica, Universitá "Federico II", Napoli and Sezione INFN Napoli, Italy.*
dettorre@na.infn.it

Abstract: the ARGO-YBJ experiment is in stable data taking since November 2007 at the YangBaJing Cosmic Ray Laboratory (Tibet, P.R. China, 4300 m a.s.l., 606 g/cm^2). The results from the first three years of operation are reviewed.

Keywords: Extensive Air Showers, Cosmic Rays, ARGO-YBJ experiment

1 Introduction

The ARGO-YBJ detector is in stable data taking since November 2007 with a duty cycle $>$85% and with excellent performance. The experiment, promoted and funded by the Italian Institute for Nuclear Physics (INFN) and by the Chinese Academy of Sciences (CAS) in the framework of the Italy-China scientific cooperation, is operating at the YangBaJing Cosmic Ray Laboratory (Tibet, P.R. China, 4300m a.s.l., 606 g/cm^2).

Location and detector features make ARGO-YBJ capable of investigating a wide range of fundamental issues in Cosmic Ray and Astroparticle Physics at a relatively low energy threshold:

- high energy γ-ray astronomy, at an energy threshold of a few hundred GeV;
- search for emission of gamma ray bursts in the full GeV-TeV energy range;
- cosmic rays physics (energy spectrum, chemical composition, $\overline{p}/p$ ratio measurement, shower space-time structure, multicore events, p-air and pp cross section measurement) starting from TeV energies;
- Sun and heliosphere physics above $\sim$1 GeV.

In the following sections, after a description of the detector and its performance, the main results achieved after about 3 years of stable data taking are reviewed.

2 The ARGO-YBJ experiment

The ARGO-YBJ experiment is currently the only air shower array with a dense sampling active area operated at high altitude, with the aim of studying the cosmic radiation at an energy threshold of a few hundred GeV. The large field of view ($\sim$2 sr) and the high duty cycle ($\geq$85%) allow a continuous monitoring of the sky in the declination band from -10° to 70°.

The detector is composed of a central carpet large $\sim$74$\times$ 78 m^2, made of a single layer of Resistive Plate Chambers (RPCs) with $\sim$93% of active area, enclosed by a guard ring partially ($\sim$20%) instrumented with RPCs up to $\sim$100$\times$110 m^2. The apparatus has a modular structure, the basic data acquisition element being a cluster (5.7$\times$7.6 m^2), made of 12 RPCs (2.8$\times$1.25 m^2 each). Each chamber is read by 80 external strips of 6.75$\times$61.8 cm^2 (the spatial pixels), logically organized in 10 independent pads of 55.6$\times$61.8 cm^2 which represent the time pixels of the detector. The read-out of 18360 pads and 146880 strips is the digital output of the detector [1]. The relation between strip and pad multiplicity has been measured and found in fine agreement with the Monte Carlo (MC) prediction [1]. In addition, in order to extend the dynamical range up to PeV energies, each chamber is equipped with two large size pads (139$\times$123 cm^2) to collect the total charge developed by the particles hitting the detector. The high granularity of the detector readout allows a detailed reconstruction of the space-time profile of the shower front and of the charge distribution around the core. The RPCs are operated in streamer mode by using a gas mixture (Ar 15%, Isobutane 10%, TetraFluoroEthane 75%) for high altitude operation. The high voltage set at 7.2 kV ensures an overall efficiency of about 96% [2]. The central carpet contains 130 clusters (hereafter, ARGO-130) and the full detector is composed of 153 clusters for a total active surface of $\sim$6700 m^2. ARGO-YBJ operates in two independent acquisition modes: the *shower mode* and the *scaler mode*. In shower mode, for each event the location and timing of every detected particle is recorded, allowing the reconstruction of the lateral distribution and the arrival direction [3]. In scaler mode the total counts on each cluster are measured every 0.5 s, with limited information on both the space dis-

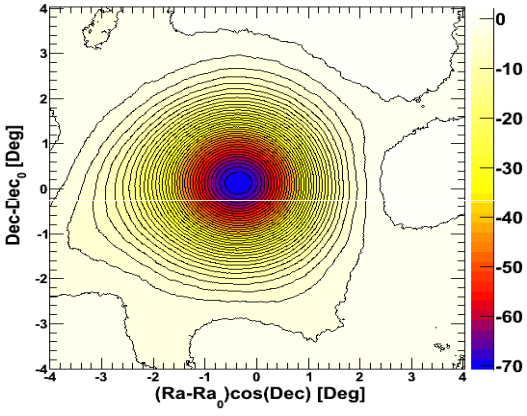

Figure 1: Significance map of the Moon region for events with N_{strip} >40, observed by the ARGO-YBJ experiment in the period July 2006 - November 2010. The coordinates are right ascension and declination centered on the Moon position. The color scale gives the statistical significance in terms of standard deviations.

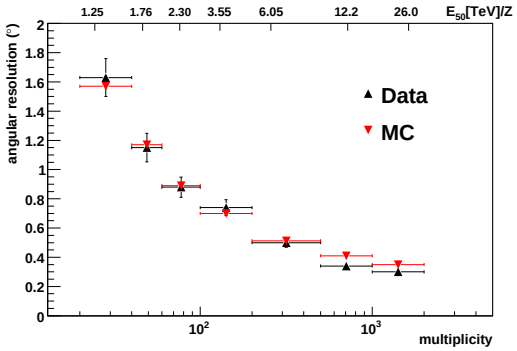

Figure 2: Measured angular resolution of the ARGO-YBJ detector compared to the expectations from MC simulation as a function of the particle multiplicity, i.e., the number of fired strips. The multiplicity bins are shown by the horizontal bars. The upper scale refers to the rigidity (TeV/Z) associated to the median energy in each multiplicity bin.

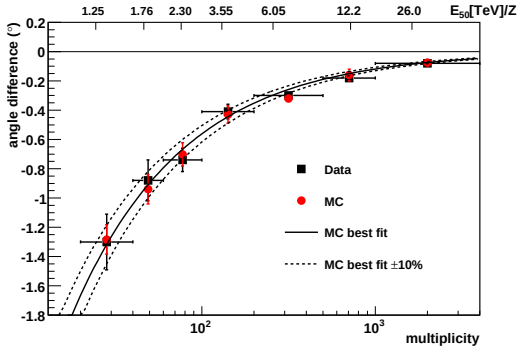

Figure 3: Measured westward displacement of the Moon shadow as a function of multiplicity (black squares). The data are compared to MC simulation (red circles). The upper scale refers to the median energy of rigidity (TeV/Z) in each multiplicity bin.

tribution and arrival direction of the detected particles, in order to lower the energy threshold down to ∼1 GeV [4]. In shower mode a simple, yet powerful, electronic logic has been implemented to build an inclusive trigger. This logic is based on a time correlation between the pad signals depending on their relative distance. In this way, all the shower events giving a number of fired pads $N_{pad} \geq N_{trig}$ in the central carpet in a time window of 420 ns generate the trigger. This can work with high efficiency down to N_{trig} = 20, keeping the rate of random coincidences negligible. The time of each fired pad in a window of 2 μs around the trigger time and its location are recorded and used to reconstruct the position of the shower core and the arrival direction of the primary particle [3]. In order to perform the time calibration of the 18360 pads, a software method has been developed [5].

The whole system, in smooth data taking since July 2006 firstly with ARGO-130, is in stable data taking with the full apparatus of 153 clusters since November 2007, with the trigger condition N_{trig} = 20. The trigger rate is ∼3.5 kHz with a dead time of 4%. All the results presented in this paper have been obtained by analysing the data collected with the digital readout.

2.1 Detector performance

The performance of the detector and the operation stability are continuously monitored by observing the Moon shadow, i.e., the deficit of cosmic rays (CR) detected in its direction. Indeed, the size of the deficit allows the measurement of the angular resolution and its position allows the evaluation of the absolute pointing accuracy of the detector. In addition, since charged particles are deflected by the geomagnetic field (GMF), the observation of the displacement of the Moon provides a direct calibration of the relation between shower size (the recorded pad/strip multiplicity) and primary energy.

ARGO-YBJ observes the Moon shadow with a sensitivity of ∼9 s.d. per month for events with a multiplicity N_{pad} ≥40 and zenith angle θ <50°, corresponding to a proton median energy E_p ∼1.8 TeV. With all data from July 2006 to November 2010 we observed the CR Moon shadowing effect with a significance of about 70 s.d. (Fig. 1). The data analysis and a full account of the results are given in [6]. The measured angular resolution is better than 0.5° for CR-induced showers with energies E > 5 TeV (Fig. 2), in excellent agreement with the MC evaluation. With the same simulation codes we find that the angular resolution for $gamma$-rays is smaller by about 30-40%, depending on the multiplicity, due to the better defined time profile of the showers.

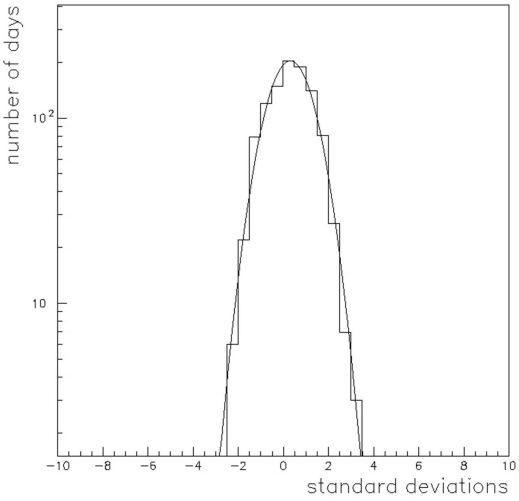

Figure 4: Significance distribution of the daily excess for 1028 days of data taking from November 2007 to October 2010, excluding 10 days around the Crab flare of September 2010.

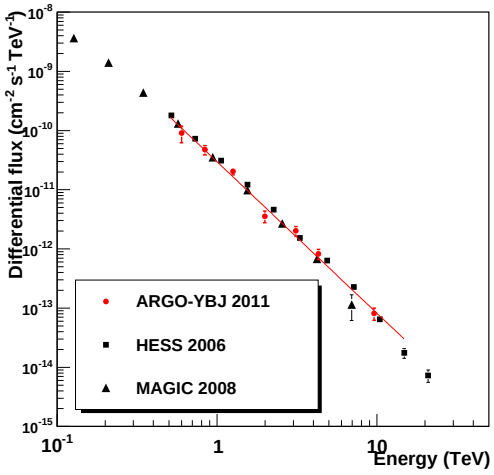

Figure 5: The Crab Nebula spectrum measured by ARGO-YBJ compared with the results of some other detectors [9, 10]. The errors reported are only statistical.

The overall absolute pointing accuracy is $\sim$0.2°. This displacement towards North is independent of the multiplicity. The most important contribution to this systematics is likely due to a residual effect not completely corrected by the time calibration procedure. The angular resolution stability is at a level of 10% in the period November 2007 - November 2010.

The relation between the observed strip multiplicity and the CR primary energy is shown in Fig. 3. The absolute energy scale uncertainty of ARGO-YBJ is estimated to be less than 13% in the energy range 1 - 30 TeV/Z [6].

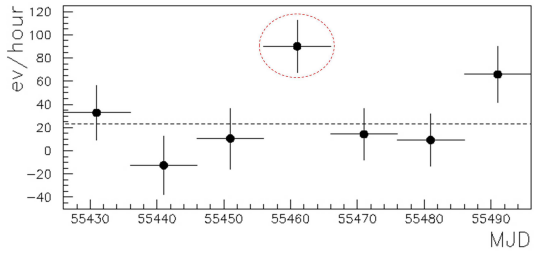

Figure 6: The rate measured in two months of data taking in bins of 10 days. The bin including the September 2010 Crab flare is showed by the red dashed circle.

3 Gamma-Ray Astronomy

With about 3 years of data we observed 4 sources with a significance greater than 5 s.d.: Crab Nebula, Mrk421, MGRO J1908+06 and MGRO J2031+41. Details on the analysis procedure (e.g., data selection, background evaluation) are given in [7, 8].

3.1 The Crab Nebula

We observed the Crab signal with a significance of 17 s.d. in about 1200 days, without any event selection to reject hadron induced showers. The statistical significance distribution of the daily excess is shown in Fig. 4. The data can be fitted with a Gaussian function with mean value 0.31$\pm$0.03 and r.m.s. = 0.99$\pm$0.02 (χ^2_ν = 1.5, degree of freedom ν = 10), showing that the detector is working with high stability and that the Crab flux is stationaty on the daily scale over the whole period. According to MC simulations, 84% of the detected events comes from primary photons of energies greater than 300 GeV, while only 8% comes from primaries above 10 TeV. The lowest energy point of the Crab Nebula spectrum shown in Fig. 5 is at a median energy of 620 GeV. The observed flux is consistent with a steady emission, and the observed differential energy spectrum in the 0.3-30 TeV range is dN/dE = $(3.0\pm0.3_{stat})\cdot10^{-11}\cdot$ (E/1 TeV)$^{-2.57\pm0.09_{stat}}$ cm^{-2} s^{-1} TeV^{-1} in agreement with other measurements [9, 10]. From these data we obtain that after 3 years of data taking the integrated sensitivity of ARGO-YBJ, without any rejection of the hadronic background, is of 0.3 Crab units.

The Crab featured a large γ-ray flare on September 18, 2010 reported by the AGILE and Fermi Collaborations [11, 12]. A flux enhancement by a factor 4 in coincidence with this flare has been observed by ARGO-YBJ as shown in Fig. 6. The increase of the counting rate starts two days before the onset detected by AGILE and persists for 10 days. The observed flux increase corresponds to 4.1 s.d. excess above the background, to be compared to an average expected steady Crab flux of about 1.0 s.d. .

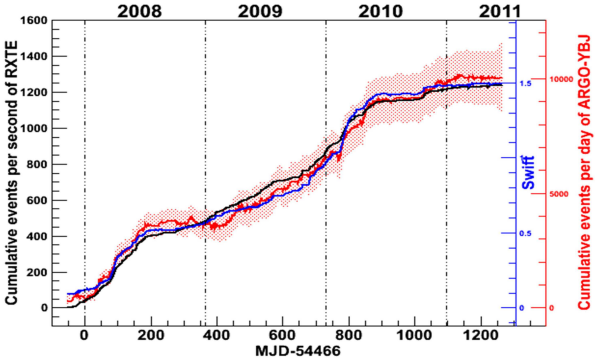

Figure 7: Cumulative light curve from Mrk421 measured by ARGO-YBJ (red curve) compared with RXTE/ASM (black curve) and Swfit (blue curve) X-ray data. The shaded red region indicates the corresponding 1σ statistical error.

?

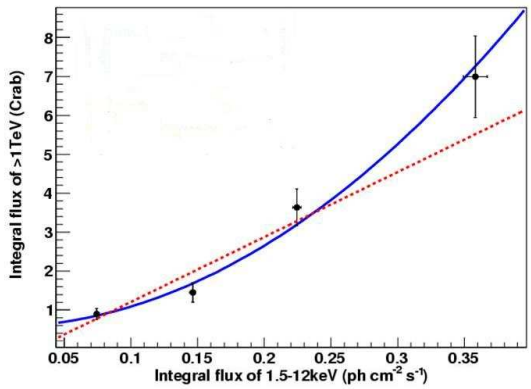

Figure 8: ARGO-YBJ >1 TeV flux (in Crab units) vs. RXTE/ASM X-ray flux. Solid line: quadratic best-fit. Dotted line: linear best-fit.

This flux variability has not been confirmed by the sparse observations of VERITAS (6 observations of about 20 mins each) and MAGIC (one observation of about 58 mins) during the duration of the flare. Thus, these results do not support the ARGO-YBJ findings. An increase of the flux (a 3.5 s.d. signal to be compared to an expected excess of 0.62 s.d.) has been also detected in coincidence with the flare detected by Fermi and AGILE in April 2011. No Cherenkov data are available for this event.

Finally, no evidence of a flux enhancement is observed during the flare detected by Fermi in February 2009.

In conclusion, the ARGO-YBJ data show a marginal evidence of a TeV flux increase correlated to the MeV-GeV flaring activity, with a statistical significance not enough to draw a firm conclusion. Further efforts to improve the data reconstruction and the data analysis exploiting the γ/h discrimination are required to better understand the observed phenomenology.

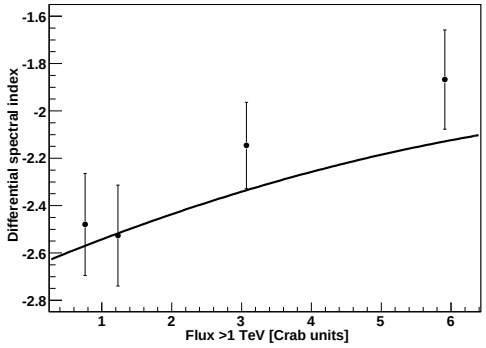

Figure 9: Mrk421 spectral index vs. flux above 1 TeV in Crab units. The solid line is the function obtained in [13].

3.2 The blazar Markarian 421

Mrk421 is one of the brightest blazars and the closest to us (z = 0.031), characterized by a strong broadband flaring activity with a variability time scale ranging from minutes to months. A correlation of VHE gamma rays with X-rays has been observed during single flaring episodes by different detectors and can be interpreted in terms of the Synchrotron Self-Compton (SSC) model. The Mrk421 high variability makes the long term multiwavelength observation very important to constrain the emission mechanisms models.

Mrk421 was the first source detected by the ARGO-YBJ experiment in July 2006 when the detector started recording data with only the central carpet and was in commissioning phase. ARGO-YBJ has monitored Mrk421 for more than 3 years, studying the correlation of the TeV flux with X-ray data. We observed this source with a total significance of about 12 s.d., averaging over quiet and active periods. ARGO-YBJ detected different TeV flares in correlation with X-ray observations, as can be seen in Fig. 7 where the ARGO-YBJ cumulative events per day are compared to the cumulative events per second of the RXTE/ASM and Swift satellites. The X-ray/TeV correlation is quite evident over more than 3 years. The steepness of the curve gives the flux variation, that shows an active period at the beginning of 2008, followed by a quiet phase, and in February 2010.

To get simultaneous data, 552 days have been selected for this analysis over the period from 2007 November to 2010 February. The degree of correlation and the phase difference (time lag) between the variations in X-ray and TeV bands have been evaluated using the Discrete Correlation Function (DCF) [14] that gives the correlation coefficient for two light curves as a function of the time lag between them. A quadratic correlation is found (Fig. 8) with a time lag of -0.14$^{+0.86}_{-0.85}$ and -0.94$^{+1.05}_{-1.07}$ days for RXTE/ASM and Swift data, respectively. Therefore, no significant time lag is found between X-ray data and TeV ARGO-YBJ observations.

The extended data set allows to study the relation between the flux and the TeV spectral index. The TeV flux measured by ARGO-YBJ ranges from 0.9 to about 7 Crab units. As shown in Fig. 9 the TeV spectral index hardens with increasing flux in agreement with the results obtained by the Whipple collaboration in 2002 (continuous line) [13]. This conclusion generalizes the ARGO-YBJ result obtained with the analysis of the June 2008 flare [7]. The temporal and the spectral analysis strongly support the predictions of the one-zone SSC model. A full account of this analysis can be found in [8].

3.3 MGRO J1908+06

The gamma ray source MGRO J1908+06 was discovered by MILAGRO [15] at a median energy of $\sim$ 20 TeV and recently associated with the Fermi pulsar 0FGL J1907.5+0602 [16]. The data were consistent both with a point source and with an extended source of diameter $<$ 2.6°. HESS confirmed the discovery with the detection of the extended source HESS J1908+063 [17] at energies above 300 GeV, positionally consistent with the MILAGRO source. The extension of the source was extimated σ_{ext} = $0.34^{\circ}{}^{+0.04}_{-0.03}$. The MILAGRO and HESS fluxes are in disagreement at a level of 2-3 s.d., the MILAGRO result being about a factor 3 higher at 10 TeV [18].

ARGO-YBJ observed a TeV emission from MGRO J1908+06 with a significance greater than 5 s.d. in a total on-source time of 5358 hours, Fig. 10. At the ARGO-YBJ site, MGRO J1908+06 culminates at the relatively low zenith angle of 24° and is visible for 5.4 hours per day with a zenith angle less than 45°. By assuming a 2D Gaussian source shape with r.m.s = σ_{ext}, we fitted the event distribution as a function of the distance from the center (set to the HESS source position) and, taking into account the Point Spread Function (PSF), we found σ_{ext}=0.50$\pm$0.35, a value larger but consistent with the HESS measurement.

The best fit power law spectrum is: dN/dE = 2.2$\pm$0.4$\times$ 10^{-13} (E/7 TeV)$^{-2.3\pm0.3}$ photons cm^{-2} s^{-1} TeV^{-1} (the errors on the parameters are statistical) (Fig. 11). The systematic errors are mainly related to the background evaluation and to the uncertainty in the absolute energy scale. According to our estimate, they globally affect the quoted fluxes for $\leq$ 30%. Given the flat slope, above a few TeV the MGRO J1908+06 flux becomes larger than the Crab Nebula one. A significant disagreement appears between the ARGO-YBJ and HESS fluxes. In the limit of the statistical accuracy of this result, our data support the MILAGRO measurement of a flux significantly larger than that measured by HESS. One possible cause of this discrepancy is that ARGO-YBJ and MILAGRO integrate the signal over a solid angle larger than the HESS one, and likely detect more of the diffuse lateral tail of the extended source. A contribution is expected from the diffuse gamma-ray flux produced by cosmic rays interacting with matter and radiation in the Galaxy. According to the prediction of the "optimized" GALPROP model [20, 21], confirmed by a MILAGRO measurement at 15 TeV [22], the amount of this contribution to the measured flux from MGRO J1908+06 at a few TeV is estimated 15$-$20%, and cannot account for the entire observed disagreement.

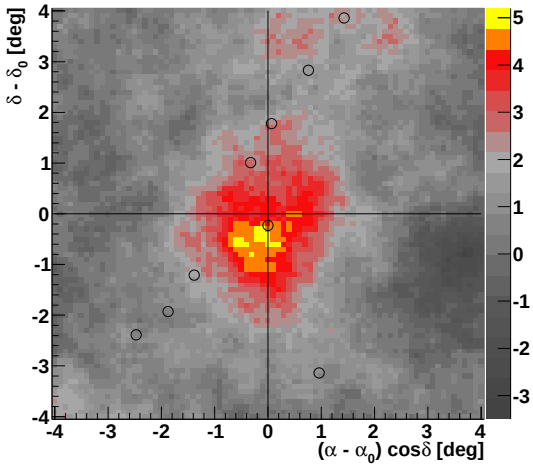

Figure 10: Significance map of the 8° $\times$ 8° region around MGROJ1908+06 obtained by ARGO-YBJ, for events with N_{pad} $\geq$40. The center of the map represents the position of the HESS source. The open circles show the positions of the gamma-ray sources observed by Fermi in the same region [19].

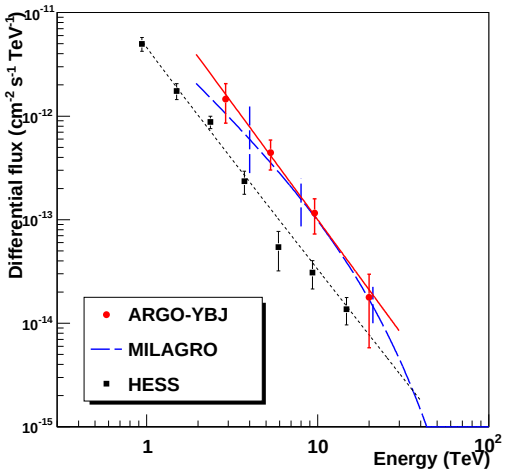

Figure 11: Differential flux from MGRO J1908+06 measured by different detectors: ARGO-YBJ (red points, with best fit given by the line); MILAGRO (the blue dashed line gives the fit and the vertical lines are the 1 s.d. errors at some values of the energy); HESS (black squares, with best fit given by the line). The plotted errors are purely statistical for all the detectors.

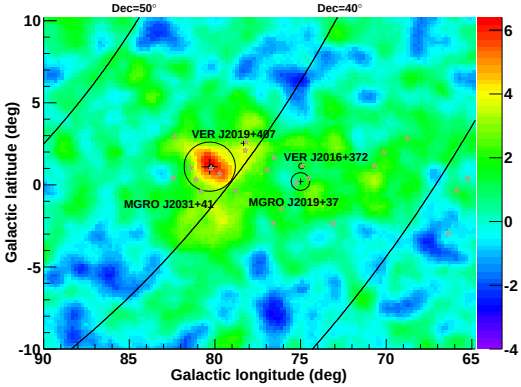

Figure 12: Significance map of the Cygnus Region as observed by the ARGO-YBJ experiment. The four known VHE γ-ray source are reported. The errors on the MGRO source positions are marked with crosses, while the circles indicate their intrinsic sizes [15, 23]. The cross for VER J2019+407 indicates its extension [24]. The source VER J2016+372 is marked with small circles without position errors. The small circle within the errors of MGROJ2031+41 indicates position and extension of the source TeV J2032+4130 as estimated by the MAGIC collaboration [25]. The open stars mark the location of the 24 GeV sources in the second $Fermi$ LAT catalog.

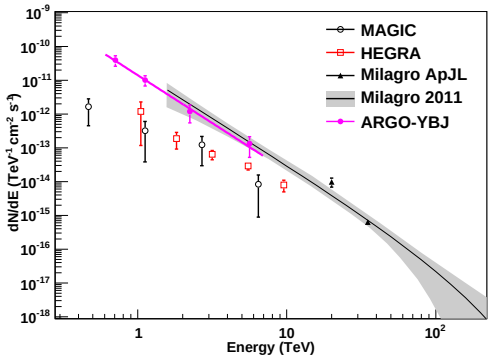

Figure 13: Energy density spectrum from TeV J2032+4130/MGRO J2031+41 as measured by the ARGO-YBJ experiment (magenta solid line). The spectral measurements of HEGRA [26] and MAGIC [25] are also reported for comparison. The solid line and shaded area indicate the differential energy spectrum and the 1 s.d. error region as recently determined by the Milagro experiment [27]. The two triangles give the previous flux measurements by Milagro at 20 TeV [15] and 35 TeV [16].

3.4 MGRO J2031+41 and the Cygnus region

The Cygnus region contains a large column density of interstellar gas and is rich of potential cosmic ray acceleration sites as Wolf-Rayet stars, OB associations and supernova remnants. Several VHE gamma-ray sources have been discovered within this region in the past decade,including two bright extended sources detected by the Milagro experiment.

The gamma ray source MGRO J2031+41 was detected by MILAGRO [15] at a median energy of $\sim$ 20 TeV, is spatially consistent with the source TeV J2032+4130 discovered by the HEGRA collaboration [28, 26] and likely associated with the Fermi pulsar 1FGL J2032.2+4127 [29]. The extension measured by MILAGRO, 3.0°$\pm$0.9°, is much larger than that initially estimated by HEGRA (about 0.1°).

The bright unidentified source MGRO J2019+37 is the most significant source in the Milagro data set apart from the Crab Nebula. This is an enigmatic source due to its high flux not being confirmed by other VHE gamma-ray detectors. The Cygnus region has been studied by the ARGO-YBJ experiment by using data collected from 2007 November through 2011 August. The results of the data analysis are shown in Fig. 12 e Fig. 13 . A TeV emission from a position consistent with TeV J2032+4130/MGRO J2031+41 is found with a significance of 6.4 s.d. .

The intrinsic extension of this emission results to be about 0.2°, a value consistent with the estimation by HEGRA (and MAGIC [25]). Assuming σ_{ext}=0.1 the integral flux above 1 TeV is about 30% that of the Crab Nebula, which is much higher than the flux of TEV J2032+4130 as determined by HEGRA (5%) and MAGIC (3%).

The reason for the large discrepancy between the fluxes measured by Cherenkov telescopes and ARGO-YBJ is still unclear. Even considering a possible contribution from a diffuse emission spreading in the Cygnus region, it is difficult to explain this discrepancy.

On the contrary, no evidence of a TeV emission above 3 s.d. is found at the location of MGRO J2019+37. At energies above 5 TeV the ARGO-YBJ exposure is still insufficient to reach a firm conclusion while at lower energies the ARGO-YBJ upper limit is marginally consistent with the spectrum determined by Milagro [30]. The observation of ARGO-YBJ is about five years later than that by Milagro. Given the estimated source radius of 4-15 pc, a flux variation over a smaller region in the source area cannot be completely excluded, such scenario, however, making impossible to identify MGRO J2019+37 as a pulsar wind nebula.

3.5 Diffuse emission from the Galactic Plane

Diffuse gamma rays are produced by relativistic electrons by bremsstrahlung or by inverse Compton scattering on background radiation fields, or by protons and nuclei via the decay of pai-zero produced in hadronic interactions with interstellar gases. Thus the space distribution of this emission can trace the location of the cosmic ray sources and the distribution of interstellar gases. Gamma rays at energies above 200 GeV near the Galactic center have been observed by the HESS telescope [31]. A diffuse gamma ray flux at energies around 15 TeV from the $30° < l < 110°$ longitudine range of the Galactic plane has been reported

by Milagro [22]. A very preliminary analysis of the events collected by ARGO-YBJ in about 4 years of data taking evidences a diffuse emission at energies >300 GeV from the inner Galactic plane ($25° < l < 85°, |b| < 2°$) with a measured flux $E^2 \cdot dN/dE = 1 \div 1.5 \cdot 10^{-9}$ [32].

3.6 Gamma Ray Bursts

Working in scaler mode [4] ARGO-YBJ has performed a search for high energy emission from GRBs collecting data from November 2004 (corresponding to the Swift satellite launch) to April 2011, with a detector active area increasing from ∼700 to ∼6700 m^2. During this period, a total of 131 GRBs was inside the ARGO-YBJ field of view (i.e. with zenith angle $\theta \leq 45°$, limited only by atmospheric absorption); for 110 of these ARGO-YBJ data were available and they have been investigated by searching for a significant excess in the counting rates coincident with the satellite detection. In order to extract the maximum information from the data, two GRB analyses have been implemented:

- search for a signal from every single GRB;
- search for a signal from the pile-up of all GRBs (stacked analysis).

In the search for GeV gamma rays in coincidence with the low energy GRBs detected by satellites, no evidence of emission was found for any event. The stacked search, both in time and phase, has shown no deviation from the statistical expectations, therefore excluding any integral effect.

The fluence upper limits obtained in the 1-100 GeV energy range depend on the zenith angle, time duration and spectral index, reaching values down to 10^{-5} erg cm^{-2}. These values greatly depend on the energy range of the calculation. If we consider our sensitivity in terms of expected number of positive detections, our estimate gives a rate between 0.2 and 1 per year [4], which is comparable with similar evaluations for other experiments working in different energy regions (e.g. [33]). Finally, the capability of the detector in shower mode to measure the arrival direction and energy of individual showers above a few hundred GeV allows the ARGO-YBJ experiment to study the GRBs in the whole 1 GeV - 1 TeV range. A detailed discussion on the methods and the first published results can be found in [34, 35].

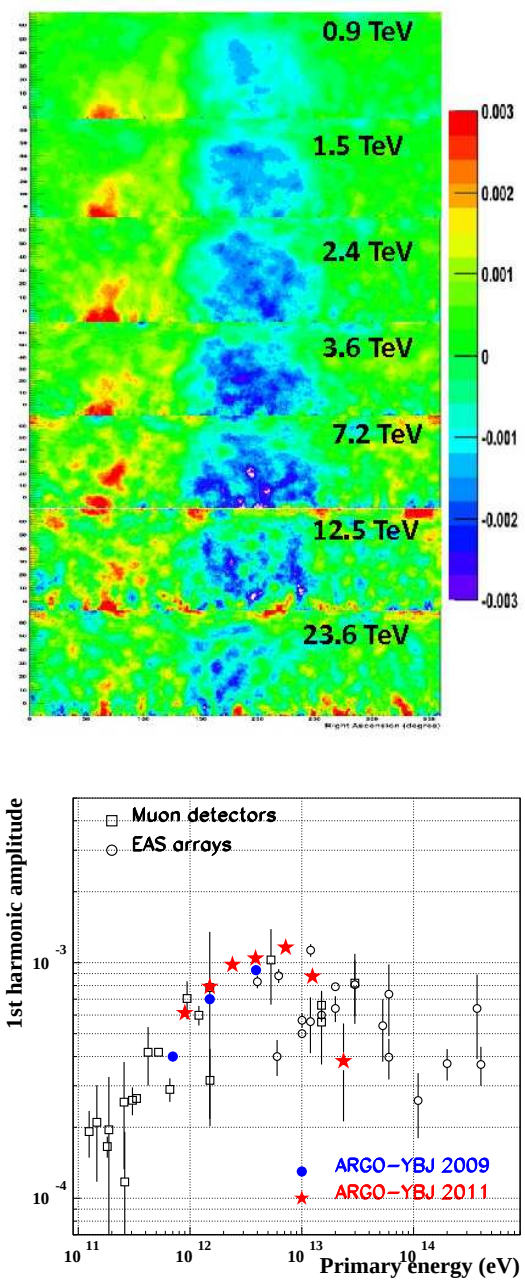

Figure 14: Upper plot: Large scale CR anisotropy observed by ARGO-YBJ as a function of the energy. The color scale gives the relative CR intensity. Lower plot: Amplitude of the first harmonic as a function of the energy, compared to other measurements.

4 Cosmic Ray Physics

4.1 Large and Medium scale anisotropies

The intensity of cosmic rays at TeV energies is nearly isotropic due to the Galactic magnetic fields which randomize and scramble their arrival directions. However, extensive observations show that there exist a slight anisotropy of $\approx 10^{-3}$ [36]. In addition the relative intensity map of the cosmic ray flux exhibits some localized regions of significant excess in both hemispheres [37, 38].

To study the anisotropy at different angular scales the isotropic background of CRs has been estimated with two well-known methods: the equi-zenith angle method [39] and the direct integration method [40]. The equi-zenith angle method, used to study the large scale anisotropy, is able to eliminate various spurious effects caused by instrumental and environmental variations, such as changes in pressure and temperature that are hard to control and tend to introduce systematic errors in the measurement. The di-

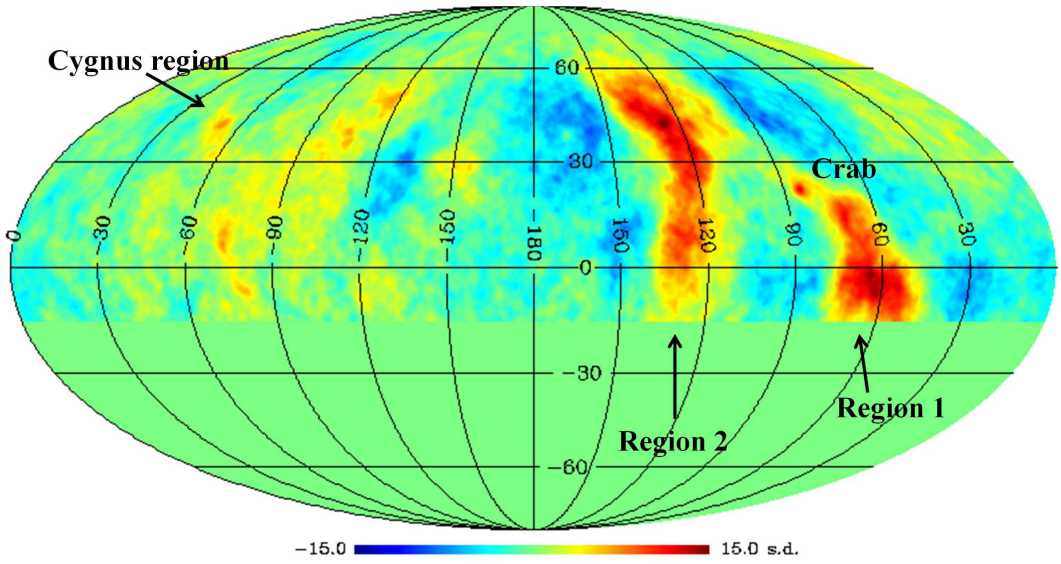

Figure 15: Medium scale CR anisotropy observed by ARGO-YBJ. The color scale gives the statistical significance of the observation in standard deviations.

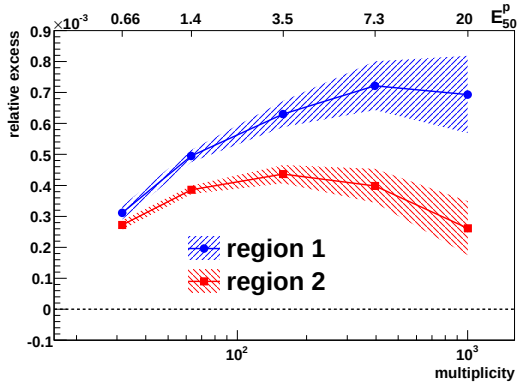

Figure 16: Size spectrum of the regions 1 and 2. The vertical axis represents the relative excess (Ev-Bg)/Bg. The upper scale shows the corresponding proton median energy. The shadowed area represents the 1σ error band.

rect integration method, based on time-average, relies on the assumption that the local distribution of the incoming CRs is slowly varying and the time-averaged signal may be used as a good estimation of the background content. Time-averaging methods act effectively as a high-pass filter, not allowing to inspect features larger than the time over which the background is computed (i.e., 15°/hour$\times\Delta t$ in R.A.). The time interval used to compute the average spans Δt= 3 hours and makes us confident that the results are reliable for structures up to ≈35° wide.

The observation of the CR large scale anisotropy by ARGO-YBJ is shown in the upper plot of Fig. 14 as a function of the primary energy up to about 25 TeV. The data used in this analysis were collected by ARGO-YBJ from 2008 January to 2009 December with a reconstructed zenith angle $\leq$ 45°. The so-called *'tail-in'* and *'loss-cone'* regions, correlated to an enhancement and a deficit of CRs, are clearly visible with a statistical significance greater than 20 s.d.. The tail-in broad structure appears to dissolve to smaller angular scale spots with increasing energy. To quantify the scale of the anisotropy we studied the 1-D R.A. projections integrating the sky maps inside a declination band given by the field of view of the detector. Therefore, we fitted the R.A. profiles with the first two harmonics. The resulting amplitude of the first harmonic is plotted in the lower plot of Fig. 14 where is compared to other measurements as a function of the energy. The ARGO-YBJ results are in agreement with other experiments suggesting a decrease of the anisotropy first harmonic amplitude with increasing energy.

The Fig. 15 shows the ARGO-YBJ sky map in equatorial coordinates. The analysis refers to events collected from November 2007 to May 2011 after the following selections: (1) $\geq$25 shower particles on the detector; (2) zenith angle of the reconstructed showers $\leq$50°. The triggering showers that passed the selection were about $2{\cdot}10^{11}$. The zenith cut selects the declination region $\delta \sim$ -20° ÷ 80°. According to the simulation, the median energy of the isotropic cosmic ray proton flux is E_p^{50} ≈1.8 TeV (mode energy ≈0.7 TeV).

The most evident features are observed by ARGO-YBJ around the positions $\alpha \sim 120°$, $\delta \sim 40°$ and $\alpha \sim 60°$, $\delta \sim$ -5°, positionally coincident with the regions detected by Milagro [37]. These regions, named "region 1" and "region 2", are observed with a statistical significance of about 14 s.d.. The deficit regions parallel to the excesses are due to a known effect of the analysis, that uses also

the excess events to evaluate the background, artificially increasing the background. On the left side of the sky map, several possible new extended features are visible, though less intense than those aforementioned. The area $195° \leq R.A. \leq 315°$ seems to be full of few-degree excesses not compatible with random fluctuations (the statistical significance is more than 6 s.d. post-trial). The observation of these structures is reported here for the first time and together with that of regions 1 and 2 it may open the way to an interesting study of the TeV CR sky. To figure out the energy spectrum of the excesses, data have been divided into five independent shower multiplicity sets. The number of events collected within each region are computed for the event map (Ev) as well as for the background one (Bg). The relative excess (Ev-Bg)/Bg is computed for each multiplicity interval. The result is shown in Fig. 16. Region 1 seems to have spectrum harder than isotropic CRs decreasing above 600 shower particles (proton median energy E_p^{50} = 8 TeV). On the other hand, the excess hosted in region 2 is less intense and seems to have a spectrum more similar to that of isotropic cosmic rays. We remark that, in order to filter the global anisotropy, we upplied a method similar to the one used by Milagro and Icecube. Further studies using different approaches are on the way.

4.2 Measurement of the light component spectrum of CRs

Protons and Helium nuclei are the bulk of the cosmic rays at energies below the knee ($\sim 3 \cdot 10^{15}$eV). Recent precise measurements carried out by the long duration flights of the balloon-borne CREAM experiment show that the energy spectra of this light component from 2.5 TeV to 250 TeV are flatter than the spectra measured at lower energies [42]. Since the evolution of the proton and Helium energy spectra and their subtle differences can be an indication of different population of cosmic ray sources or acceleration sites, measurements performed by different techniques can be useful as cross-check of results concerning absolute fluxes and spectral indices. The ARGO-YBJ experiment is able to overlap direct measurements in a wide region below 100 TeV, not accessible by other extensive air shower experiments.

The differential energy spectrum of the primary CR light component (p+He) measured by ARGO-YBJ (filled triangles) in the energy region 5 - 250 TeV by using a Bayesian unfolding approach is compared with the results of other experiments in Fig. 17. We selected showers with zenith angle θ <30° and with reconstructed core position inside a fiducial area 50×50 m^2 large by applying a selection criterion based on the particle density. In the energy range investigated the contamination of heavier nuclei is found to be negligible, not exceeding a few percent. The ARGO-YBJ data agree are fairly consistent with the values obtained by adding up the proton and helium fluxes measured by CREAM concerning both the total intensities and the spectrum [41]. The disagreement with the flux of the

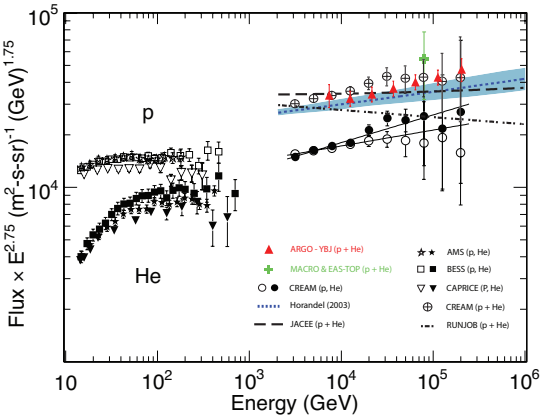

Figure 17: The differential energy spectrum of the light component (proton and Helium) measured by ARGO-YBJ (filled red triangles) compared with the proton (open circles) and Helium spectrum (filled circles) measured by the CREAM experiment [41]. The crossed circles represent the sum of the proton and Helium data measured by CREAM [42]. The blue dotted line represents the best fit to proton and Helium data quoted by Hörandel [43], and the shaded area is obtained considering the errors on the fit parameters. The dashed line represents the JACEE proton and Helium measurements [44], the dot-dashed line represents the RUNJOB proton and Helium measurements [45] (the errors on both are not reported). The green cross represents the proton and Helium flux measured by EAS-TOP and MACRO collaborations [46]. The spectra obtained at lower energies by AMS (stars, [47]), BESS (squares, [48]) and CAPRICE (inverted triangles, [49]) are also shown.

light component quoted by RUNJOB is remarkable. The value of the spectral index of the power-law fit representing the ARGO-YBJ data is -2.61±0.04, which should be compared to γ_p = -2.66±0.02 and γ_{He} = -2.58±0.02 obtained by CREAM. The present analysis does not allow the determination of the individual proton and helium contributions to the measured flux, however the ARGO-YBJ data are mainly induced by protons since the average energy of helium primaries contributing to events with a given multiplicity is about 1.5 - 2 times greater than the average proton energy. This result suggests a possible hardening of the proton spectrum at energies >5 TeV with respect to that obtained at lower energies from direct measurements with satellites and balloon-borne detectors. We emphasize that for the first time direct and ground-based measurements overlap over a wide energy range thus making possible the cross-calibration of the different experimental techniques.

4.3 Measurement of the $\overline{p}/p$ ratio at TeV energies

In order to measure the $\overline{p}/p$ ratio at TeV energies we exploit the Earth-Moon system as an ion spectrometer: if protons are deflected towards East, antiprotons are deflected towards West. If the energy is low enough and the angular

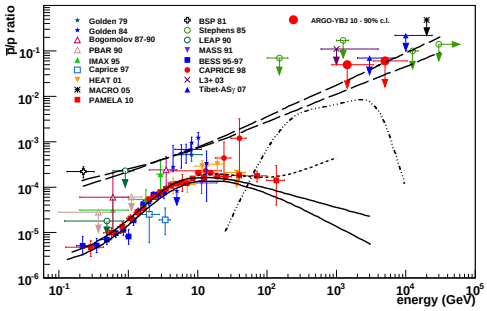

Figure 18: The $\overline{p}/p$ flux ratio obtained with the ARGO-YBJ experiment compared with all the available measurements [50, 51, 52, 53, 54] and some theoretical expectations. The solid curve refers to a calculation for a pure secondary production of antiprotons during the cosmic ray propagation in the Galaxy [55]. The dashed lines refer to a model of primary $\overline{p}$ production by antistars [56]. The confinement of cosmic rays in the Galaxy is assumed to be dependent on the rigidity R as $\propto R^{-\delta}$, and the two curves represent the cases for δ=0.6 (upper) and 0.7 (lower). The dotted line refers to the contribution of antiprotons from the annihilation of a heavy dark matter particle [57]. The dot-dashed line shows the calculation for secondary antiprotons including an additional $\overline{p}$ component produced and accelerated at cosmic ray sources [58].

resolution is adequate we could distinguish, in principle, two shadows, one shifted towards West due to the protons and the other shifted towards East due to the antiprotons. If no event deficit is observed on the antimatter side an upper limit on the antiproton content can be calculated.

We selected 2 multiplicity bins, 40<N<100 and N>100. In the first interval the statistical significance of the Moon shadow is 34 s.d., the measured angular resolution is $\sim 1^\circ$ and the median energy is 1.4 TeV. For N>100 the significance is 55 s.d., the angular resolution is $\sim 0.6^\circ$ and the median energy is 5 TeV. Taking into account that at these energies protons are about 70% of the total flux, with all the data up to December 2009 we are able to set two upper limits to the $\overline{p}/p$ ratio at the 90% confidence level: 5% at 1.4 TeV and 6% at 5 TeV, assuming for the antiprotons the proton spectral index.

The upper limits obtained by ARGO-YBJ are compared in Fig. 18 to all the available $\overline{p}/p$ measurements and to some theoretical models for antiproton production. The solid curves refer to a direct production model. The dashed lines refer to a model of primary $\bar{p}$ production by antigalaxies [59]. The rigidity-dependent confinement of cosmic rays in the Galaxy is assumed to be $\propto \mathrm{R}^{-\delta}$, being R the rigidity, and the two dashed curves correspond to the cases of δ = 0.6 and 0.7. The dotted line refers to a possible contribution from the annihilation of a heavy Dark Matter particle [57]. We note that in the few-TeV range the ARGO-YBJ results are the lowest available, useful to constrain models for antiproton production in antimatter domains.

4.4 Measurement of the total p-p cross section

To make this measurement, the ARGO-YBJ data analysis is based on the study of the shower flux attenuation for different zenith angles, i.e. atmospheric depths, and exploits the detector accuracy in reconstructing the shower properties. For fixed primary energy and shower age, such an attenuation is expressed by the absorption length, Λ, connected to the primary (mainly protons) interaction length in the atmosphere by the relation: $\Lambda = k \cdot \lambda_{CR}$, where k depends on the shower development in the atmosphere, on its fluctuations and on the detector response. The actual value of k must be evaluated by MC simulations, and it might in principle depend on the features of the adopted hadronic interaction model, even if several studies showed that the dependence is small. For primary protons, the interaction length is related to the p-air interaction cross-section by: $\lambda_p(g/cm^2) \simeq 2.41{\cdot}10^4/\sigma_{p-air}$ (mb). The measurement is accessed by selecting showers with the maximum development not far from the detection level and, obviously, exploring a zenith angle region as wide as possible. With these objectives, the ARGO-YBJ detector location (that is small atmospheric depth) and its features (full coverage, angular resolution, fine granularity, etc.), which ensure the capability of reconstructing the detected showers in a very detailed way, have been exploited (see [60] for the analysis details).

The measured p-air production cross section as a function of the primary proton energy is reported in Fig. 19. The results found by other experiments an the predictions of several hadronic interaction models are also shown. The systematics arising from several sources have been taken into account and evaluated on the basis of a full MC simulation. In particular, the contribution coming from heavy nuclei contained in the primary cosmic ray beam has been estimated by adding a proper helium fraction to the proton primary flux in the MC simulation (the contribution of heavier nuclei is negligible).

Finally, Glauber theory has been used to infer the total proton-proton cross section σ_{pp} from the measured proton-air production cross section σ_{p-air}. The results are shown in Fig. 20. Also shown in the figure are the measurements made at accelerators and by other CR experiments starting from σ_{p-air}. As can be seen, the ARGO-YBJ data lie in an energy region scarcely explored by accelerator experiments and permit to better investigate the behaviour of the p-p total cross section where it starts to significantly increase with energy. In particular, our result favours the asymptotic $ln^2(s)$ increase of total hadronic cross sections as obtained in [61] and [62] from a global analysis of accelerator data. The use of the analog RPC charge readout will allow to extend the study to collisions with center-of-mass energies up to the TeV region.

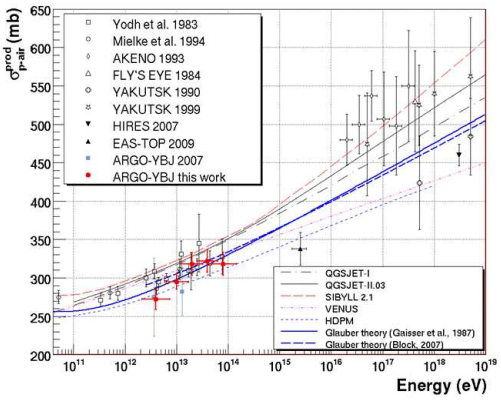

Figure 19: Proton-air production cross section measured by ARGO-YBJ and by other CR experiments. The predictions of two different calculations based on the Glauber theory are also shown. References for experimental data and theoretical predictions are given in [60].

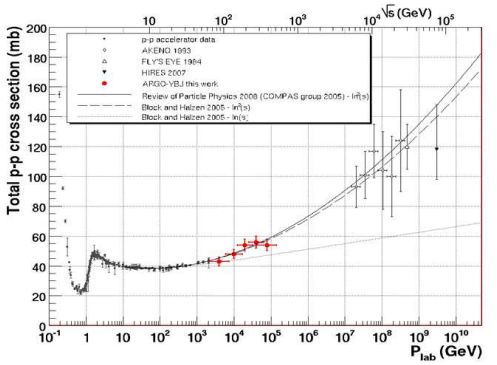

Figure 20: Total p-p cross section obtained from the σ_{p-air} cross section measured by ARGO-YBJ compared with results at accelerators and by other CR experiments (the corresponding references are given in [60]).

5 Interplanetary Magnetic Field measurement by Sun shadow

The same shadowing effect observed looking at cosmic rays in the direction of the Moon can be observed in the direction of the Sun, but the interpretation of this phenomenology is less straightforward. In fact, the displacement of the shadow from the apparent position of the Sun could be explained by the joint effects of the GMF and of the Solar and Interplanetary Magnetic Fields (SMF and IMF, respectively), whose configuration considerably changes with the phases of the solar activity cycle. In this regard, understanding the Moon shadow phenomenology is a useful tool to disentangle the effect of different magnetic fields on the Sun shadow and to performe a measurement of the IMF in a minimum of the solar activity.

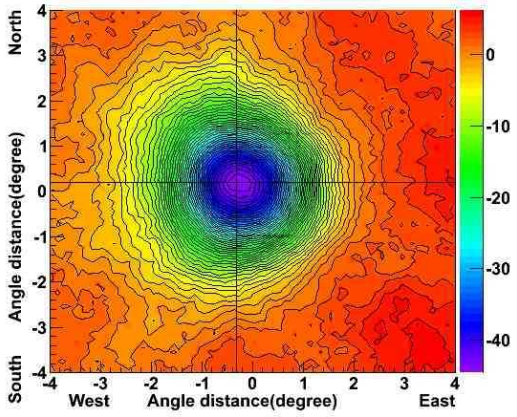

Figure 21: The Sun shadow measured using all the data taken by the ARGO-YBJ experiment from July 2006 to October 2009. The maximum significance is 44.6 s.d.. The step between contour lines is 1 s.d..

The observation using the ARGO-YBJ experiment was made just in such a particularly good time window when the solar activity stayed at its minimum for an unexpectedly long time since 2006. At distances greater than 5 solar radii from the sun centre, the IMF is distributed mainly in the ecliptic plane. Its z-component perpendicular to the ecliptic plane deflects cosmic rays in the east-west direction, therefore it drives the shadow with an extra shift in addition to the GMF effect which constantly moves the sun shadow towards west as observed in the moon shadow measurement (see Fig. 3). Its y-component, B_y, in the ecliptic plane defined to be perpendicular to the line of sight, deflects cosmic rays and thus drives the sun shadow in the north-south direction. It has no contamination from the GMF effect because the declination angle of the GMF is less than 0.5° at the ARGO-YBJ site.

The Sun shadow measured using all data taken by the ARGO-YBJ experiment from July 2006 to October 2009 is shown in Fig. 21. A detailed analysis has been carried out to study the shift of the center of the Sun shadow along the North-South direction as a function of the synodic Carrington longitude. The transverse component of the IMF, B_y, is then estimated with a minimal assumption on the model describing the IMF.

The B_y oscillates following a bi-sector or a four-sector pattern (see Fig. 22) in two periods of data taking (period 1: from January 2008 to April 2009; period 2: all the other months from July 2006 to October 2009). These patterns depend on the direction of the IMF periods that causes the deflection of the particle trajectories. The positive sign indicates that the field is pointing to the centre. The solid dots in Fig. 22 represent the measurements by the orbiting detectors (the corresponding data are available at http://omniweb.gsfc.nasa.gov). A good agreement is found after applying to the ARGO-YBJ data a phase shift of 21° corresponding to 1.6 days ahead. The two measurements

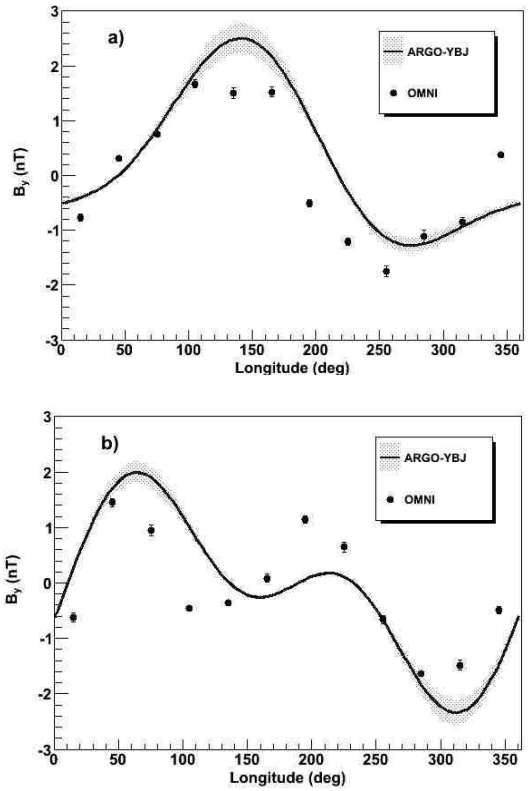

Figure 22: Comparison between two measurements of IMF using different methods. The solid curve represents the field component B_y near the Earth measured by the ARGO-YBJ experiment using CR deflection. In the period 1 (plot a)) a clear bisector pattern is observed. Positive sign indicates that the field is pointing to the centre of the Sun. An uncertainty of 1 s.d. is marked by the shaded area. The solid dots represent the measurements using the OMNI satellite network. In the plot b), the results with the 4-sector structure in the period 2 are displayed.

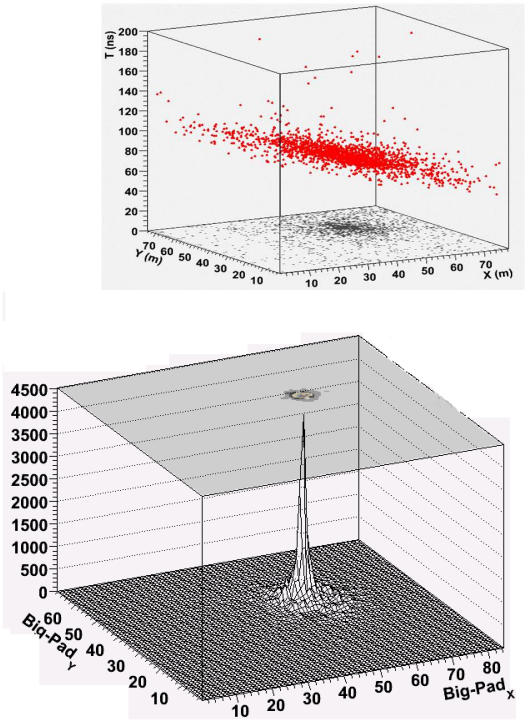

Figure 23: Showers imaged by the ARGO-YBJ central carpet with the digital (left plot: the space-time structure of a low energy shower) and the analog (right plot: the core of a high energy shower) readouts.

are of the same order in amplitude (2.0±0.2 nT) and are consistent in the alternating periodical pattern. Since relativistic CRs fly from the Sun to the Earth in only 8 minutes, they are able to take an "instantaneous" picture of IMF pattern. On the contrary, the same information is transported by the solar wind at an average speed of about 400 km s^{-1} [63].

According to this analysis, a large detector able to measure the Sun shadow with the required accuracy within one day or less, could foresee IMF disturbances which will sweep the Earth about 2 days later. Future detectors such as the LHAASO project [64] may be sufficient to carry out this measurement.

6 Conclusions

The ARGO-YBJ detector is exploiting the performance of the RPCs to image the front of atmospheric showers with unprecedented resolution and detail, as shown in Fig. 23. The digital and analog readout will allow a deep study of the CR phenomenology in the wide range from TeVs to PeVs. The results obtained in the low energy range after 3 years of data taking predict an excellent capability to address a wide range of important issues in Astroparticle Physics.

References

[1] Aielli, G. et al., Nuclear Instruments and Methods in Physics Research A, 2006, **562**: 92-96
[2] Aielli, G. et al., Nuclear Instruments and Methods in Physics Research A, 2009, **608**: 246-250
[3] Di Sciascio, G., Rossi, E. et al., Proceedings of the 30th ICRC, 2007, **4**: 123-126 (arXiv:0710.1945)
[4] Aielli, G. et al., Astroparticle Physics, 2008, **30**: 85-95
[5] Aielli, G. et al., Astroparticle Physics, 2009, **30**: 287-292
[6] Bartoli, B. et al., Physical Review D, 2011, **84**: 022003-(1-15)
[7] Aielli, G. et al., The Astrophysical Journal, 2010, **714**: L208-L212

[8] Bartoli, B. et al., The Astrophysical Journal, 2011, **734**: 110-117
[9] Aharonian, F. et al., Astronomy and Astrophysics, 2006, **457**: 899-915
[10] Albert, J. et al., The Astrophysical Journal, 2008, **674**: 1037-1055
[11] Tavani, M. et al., Science, 2011, **331**: 736-739
[12] Abdo, A. A. et al., Science, 2011, **331**: 739-742
[13] Krennrich, F. et al., The Astrophysical Journal, 2002, **575**: L9-L13
[14] Edelson, R.A., Krolik, J.H., The Astrophysical Journal, 1988, **333**: 646-659
[15] Abdo, A.A. et al., The Astrophysical Journal, 2007, **664**: L91-L94
[16] Abdo, A.A. et al., The Astrophysical Journal, 2009, **700**: L127-L131
[17] Aharonian, F. et al., Astronomy and Astrophysics, 2009, **499**: 723-728
[18] Smith, A.J. et al., 2009 Fermi Symposium and eConf Proceedings C091122 (arXiv:1001.3695)
[19] Abdo, A.A. et al., The Astrophysical Journal Supplement Series, 2010, **188**: 405-436
[20] Strong, A.W., Moskalenko, I.V., Reimer, O., The Astrophysical Journal, 2000, **537**: 763-784
[21] Porter, T.A. et al., The Astrophysical Journal, 2008, **682**: 400-407
[22] Abdo, A.A. et al., The Astrophysical Journal, 2008, **688**: 1078-1083
[23] Abdo, A.A. et al., The Astrophysical Journal, 2007, **658**: L33-L36
[24] Weinstein A., 2009 Fermi Symposium and eConf Proceedings C091122 (arXiv:0912.4492)
[25] Albert, J. et al., The Astrophysical Journal, 2008, **675**: L25-L28
[26] Aharonian, F. et al., Astronomy and Astrophysics, 2005, **431**: 197-202
[27] Bonamente E., Galbraith-Frew J., Hüntemeye P., These Proceedings, **7**: 6-8
[28] Aharonian, F. et al., Astronomy and Astrophysics, 2002, **393**: L37-L40
[29] Abdo, A.A. et al., The Astrophysical Journal Supplement Series, 2010, **187**: 460-494
[30] Abdo A.A. et al., 2012, arXiv:1202.0846
[31] Aharonian F. et al., The Astrophysical Journal, 2006, **636**: 777-797
[32] Ma L.L. et al., These Proceedings, **7**: 2-5
[33] Albert, J. et al., The Astrophysical Journal, 2007, **667**: 358-366
[34] Aielli, G. et al., The Astrophysical Journal, 2009, **699**: 1281-1287
[35] Aielli, G., et al., Astroparticle Physics, 2009, **32**: 47-52
[36] Guillian, G. et al., Physical Review D, 2007, **75**: 062003-(1-17)
[37] Abdo, A.A. et al., Physical Review Letters, 2008, **101**: 221101-(1-5)
[38] Abbasi R. et al., The Astrophysical Journal, 2011, **740**: 16-32
[39] Amenomori, M. et al., The Astrophysical Journal, 2005, **633**: 1005-1012
[40] Fleysher, R. et al., The Astrophysical Journal, 2004, **603**: 355-362
[41] Ahn, H.S. et al., The Astrophysical Journal, 2010, **714**: L89-L93
[42] Yoon, Y.S. et al., The Astrophysical Journal, 2011, **728**: 122-129
[43] Hörandel, J.R, Astroparticle Physics, 2003, **19**: 193-220
[44] Asakimori, K. et al., The Astrophysical Journal, 1998, **502**: 278-283
[45] Derbina, V.A. et al., The Astrophysical Journal, 2005, **628**: L41-L44
[46] Aglietta, M. et al., Astroparticle Physics, 2004, **21**: 223-240
[47] Aguilar, M. et al., Physics Reports, 2002, **366**: 331-405
[48] Haino, S. et al., Physics Letters B, 2004, **594**: 35-46
[49] Boezio, M., Bonvicini, V., Schiavon, P., Astroparticle Physics, 2003, **19**: 583-604
[50] Adriani, O. et al., Physical Review Letters, 2010, **105**: 121101-(1-5)
[51] Stephens, S.A., Astronomy and Astrophysics, 1985, **149**: 1-6
[52] Achard, P. et al., Astoparticle Physics, 2005, **23**: 411-434
[53] Amenomori, M. et al., Astroparticle Physics, 2007, **28**: 137-142
[54] Ambrosio, M. et al., Astroparticle Physics, 2003, **20**: 145-156
[55] Donato, F. et al., Physical Review Letters, 2009, **102**: 071301-(1-4)
[56] Stephens, S.A., Golden, R.L., Space Science Reviews, 1987, **46**: 31-91
[57] Cirelli, M. et al., Nuclear Physics B, 2009, **813**: 1-21
[58] Blasi, P., Serpico, P.D., Physical Review Letters, 2009, **103**: 081103-(1-4)
[59] Stecker, F.W. & Wolfendale, A.W., Proceedings of the 19th ICRC, 1985, **2**: 354-357
[60] Aielli, G. et al., Physical Review D, 2009, **80**: 092004-(1-14)
[61] Amsler, C. et al., Physics Letters B, 2008, **667**: 1-1340
[62] Block, M.M., Halzen, F., Physical Review D, 2005, **72**: 036006-(1-10)
[63] Aielli, G. et al., The Astrophysical Journal, 2011, **729**: 113-116
[64] Cao, Z. et al., Chinese Physics C, 2010, **34**: 249-252